PAPER

Check for updates

Environmental formaldehyde sensing at room temperature by smartphone-assisted and wearable plasmonic nanohybrids†

Andreas T. Güntner ‡*[a,b] and Florian M. Schenk‡[c]

Formaldehyde is a toxic and carcinogenic indoor air pollutant. Promising for its routine detection are gas sensors based on localized surface plasmon resonance (LSPR). Such sensors trace analytes by converting tiny changes in the local dielectric environment into easily readable, optical signals. Yet, this mechanism is inherently non-selective to volatile organic compounds (like formaldehyde) and yields rarely detection limits below parts-per-million concentrations. Here, we reveal that chemical reaction-mediated LSPR with nanohybrids of Ag/AgO_x core–shell clusters on TiO_2 enables highly selective formaldehyde sensing down to 5 parts-per-billion (ppb). Therein, AgO_x is reduced by the formaldehyde to metallic Ag resulting in strong plasmonic signal changes, as measured by UV/Vis spectroscopy and confirmed by X-ray diffraction. This interaction is highly selective to formaldehyde over other aldehydes, alcohols, ketones, aromatic compounds (as confirmed by high-resolution mass spectrometry), inorganics, and quite robust to relative humidity changes. Since this sensor works at room temperature, such LSPR nanohybrids are directly deposited onto flexible wristbands to quantify formaldehyde between 40–500 ppb at 50% RH, even with a widely available smartphone camera (Pearson correlation coefficient r = 0.998). Such chemoresponsive coatings open new avenues for wearable devices in environmental, food, health and occupational safety applications, as demonstrated by an early field test in the pathology of a local hospital.

Introduction

Nanoplasmonic materials feature distinct advantages for the design of inexpensive, low-power and wearable gas sensing devices, namely an optical read-out that can be realized sometimes even by naked eye and stable operation at room temperature.[1] To date, localized surface plasmon resonance (LSPR) sensors have been employed successfully for small inorganic molecules like H_2,[2] CO and NO_2[3] owing to their typically high concentration (*i.e.* 0.1–10 vol% for H_2) and sometimes strong interaction with the corresponding nanoparticle surfaces (*e.g.* H_2 and Pd clusters form Pd_xH_y[4]) yielding sufficient sensitivity[5] and selectivity.

Yet, the sensing of volatile organic compounds (VOC) by LSRP remains challenging and less established, despite their

high relevance for environmental monitoring,[6] non-invasive medical diagnostics[7] or food quality assessment.[8] The VOC are usually detected with conventional LSPR sensors by recognizing variations of the dielectric environment (*i.e.* refractive index changes) in the vicinity of the plasmonic nanoparticles.[9] However, this sensing mechanism is typically unable to (1) detect relevant parts-per-billion (ppb, by volume) concentrations and (2) hardly distinguishes individual VOC, due to their narrow range of refractive index variation.[10] For instance, Au metasurfaces decorated with TiO_2 nanoparticles enabled the LSPR detection of 1 vol% toluene at room temperature, but this sensor responded to other analytes (*e.g.* ethanol, acetone) quite similarly, resulting in rather low VOC selectivity.[11]

Here, we show that a chemical reaction between analyte and plasmonic surface strongly enhances the sensitivity and selectivity of LSPR sensors for individual VOC. This is investigated exemplarily with nanohybrids of Ag/AgO_x core–shell structures on TiO_2 (Fig. 1a) together with formaldehyde, a carcinogenic air pollutant[12] emitted, for instance, from wood-based products,[13] coatings or insulation materials with strict exposure limits (*e.g.* 80 ppb by WHO[14]). Therein, the AgO_x shells (yellow) undergo a redox reaction with formaldehyde vapor at room temperature.[15] This reduces the AgO_x shells to metallic Ag (black) that exhibits strong plasmonic resonance,[16] unlike AgO_x, resulting in a detectable optical signal. Note that

[a] Human-centered Sensing Laboratory, Department of Mechanical and Process Engineering, ETH Zurich, CH-8092 Zurich, Switzerland. E-mail: andregue@ethz.ch
[b] Department of Endocrinology, Diabetology, and Clinical Nutrition, University Hospital Zurich (USZ) and University of Zurich (UZH), CH-8091 Zürich, Switzerland
[c] Particle Technology Laboratory, Department of Mechanical and Process Engineering, ETH Zurich, CH-8092 Zurich, Switzerland
† Electronic supplementary information (ESI) available. See DOI: https://doi.org/10.1039/d2nr06599a
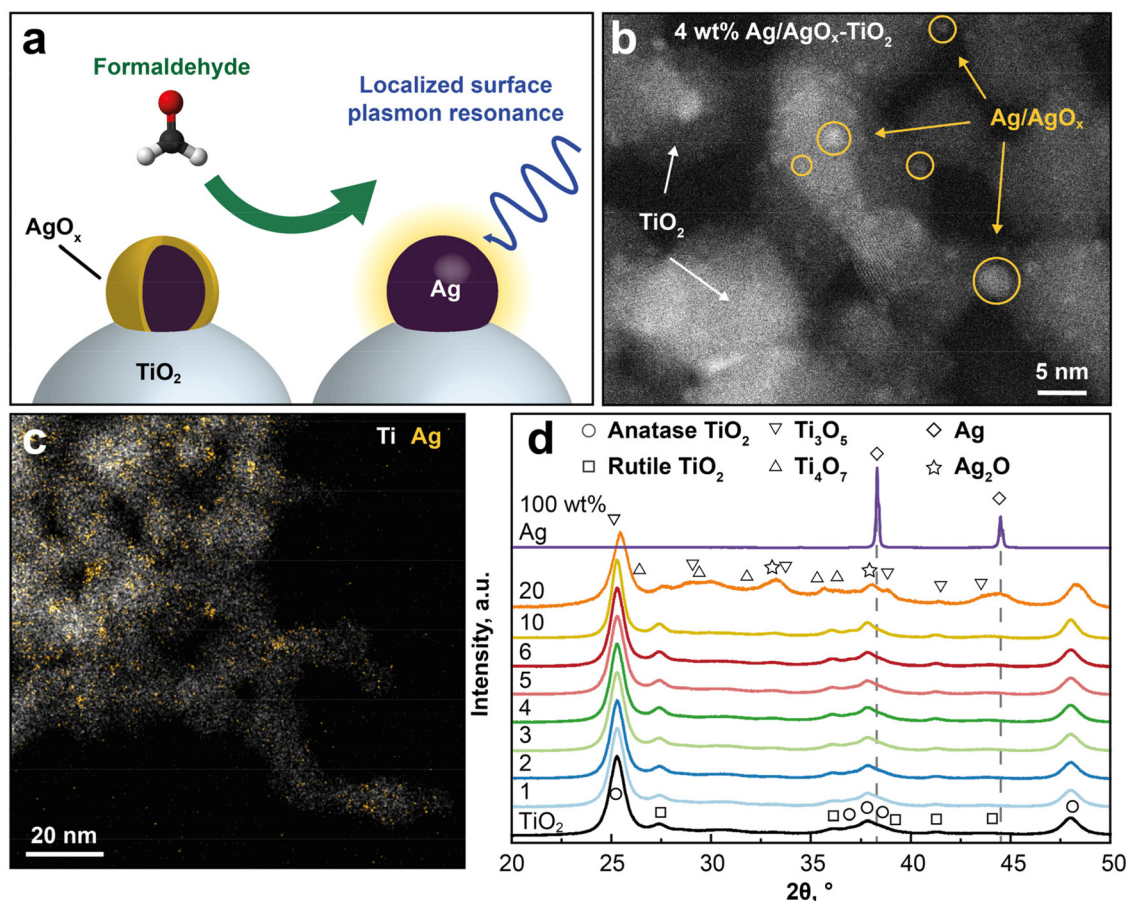‡ These authors contributed equally.
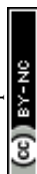
Fig. 1 Material design and characterization of Ag/AgO$_x$–TiO$_2$ nanohybrids. (a) Sensing concept and (b) HAADF-STEM (Z-contrast) image of 4 wt% Ag/AgO$_x$ on TiO$_2$ nanohybrids. (c) STEM-EDX mapping showing the elemental distribution of Ag (yellow) and Ti (white) atoms. (d) XRD patterns of annealed (500 °C for 5 h) TiO$_2$ with 0–100 wt% nominal Ag content. Reference peak positions of anatase TiO$_2$ (circles), rutile TiO$_2$ (squares), Ti$_3$O$_5$ (downward triangles), Ti$_4$O$_7$ (upward triangles), metallic Ag (diamonds) and Ag$_2$O (stars) are indicated.

the redox interaction of Ag$^+$ and aldehydes is known as the Tollens reaction,[17] that is established for the detection of aldehydes in liquids.[18]

Results and discussion

Ag/AgO$_x$–TiO$_2$ nanohybrid design

The LSPR sensing nanoparticles are prepared by single-step flame-spray pyrolysis (FSP)[19] that had yielded already well-dispersed Ag/AgO$_x$ core–shell structures on nanostructured TiO$_2$ due to strong metal support interactions for photocatalytic and antimicrobial[16] applications. In Fig. 1b, the morphology of such flame-made and annealed 4 wt% Ag/AgO$_x$ on TiO$_2$ nanohybrids is shown by scanning transmission electron microscopy with a high-angle annular dark-field detector (STEM-HAADF). Note that throughout the text, wt% refers to the nominal Ag content in the precursor (see Methods). Most importantly, Ag/AgO$_x$ clusters (some yellow-encircled in Fig. 1b) are clearly distinguished from the TiO$_2$ by their brighter appearance due to the higher scattering potential of

Ag over Ti atoms. This was confirmed also by scanning transmission electron microscopy with energy-dispersive X-ray spectroscopy (STEM-EDX) in Fig. 1c, where the elemental distribution of Ag (yellow) and Ti (white) is shown. Therein, most Ag/AgO$_x$ clusters 1–8 nm in diameter are well dispersed over the TiO$_2$ particle surfaces (Fig. 1b and ESI Fig. 1†). Also sub-nanometer-sized Ag/AgO$_x$ clusters and few larger particles (>10 nm, ESI Fig. 2†) are present, while very small clusters (<1 nm) might not be visible. Similarly flame-made Ag/AgO$_x$–SiO$_2$ had AgO$_x$ shell thickness of 1–2 atomic layers, as quantified by dissolving the AgO$_x$ in water and measuring the dissolved Ag$^+$ ions by an ion-selective electrode.[20]

Fig. 1d shows the X-ray diffraction (XRD) patterns of such powders. Most importantly, neither Ag (diamonds) nor Ag$_2$O (stars) crystals were detected for up to 10 wt% Ag/AgO$_x$. This confirms the small crystal sizes of Ag, as suggested by STEM-HAADF (Fig. 1b), and thin layer thicknesses of AgO$_x$,[20] as well as their amorphous structure. Only above 20 wt% Ag/AgO$_x$, new XRD peaks (e.g. at $2\theta = 44.5°$) emerge that indicate larger Ag crystals. Note that the characterization of the TiO$_2$ support is provided in the ESI.†
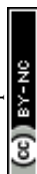
Plasmonic formaldehyde gas sensing at room temperature with Ag/AgO$_x$–TiO$_2$

Next, these 4 wt% Ag/AgO$_x$ core–shell structures on TiO$_2$ are exposed to 0–500 ppb formaldehyde at room temperature in air under realistic 50% relative humidity (RH). Fig. 2a shows the UV/Vis reflectance spectra before exposure (black line), where no distinct LSPR peak is observed. Most importantly, a plasmonic peak/hump emerges between 400 and 700 nm (with a maximum at λ_{LSPR} = 565 nm, dashed vertical line) when increasing the formaldehyde concentration up to 500 ppb, indicating reduced reflectance (or increased absorption, according to Kubelka–Munk theory[21]). Note that the small peak at 530 nm when exposed to 80 ppb formaldehyde is a measurement artifact (ESI Fig. 3a†).

The observed LSPR peak suggests the formation of surface metallic Ag through the reduction of AgO$_x$ by formaldehyde (Fig. 1a). While isolated Ag nanoparticles exhibit LSPR peaks between 400–450 nm (depending on size[22]), the red-shift here should be associated[9] to the TiO$_2$ support featuring high refractive index (e.g. anatase TiO$_2$ n = 2.54 (ref. 23)). A similar observation had been made also when exposing AgO$_x$/Ag clusters on TiO$_2$ to strong UV irradiation[16] with application as multicolor photochromic material for smart buildings or displays.[24] Consistently, AgO$_x$/Ag on SiO$_2$ with lower refractive index (i.e. n = 1.55 (ref. 23)) featured similar LSPR peak to isolated Ag (i.e. 405 nm, ESI Fig. 4†).

By quantifying the reflectance change at λ_{LSPR} (i.e. response ΔR), formaldehyde concentrations are detected over the entire
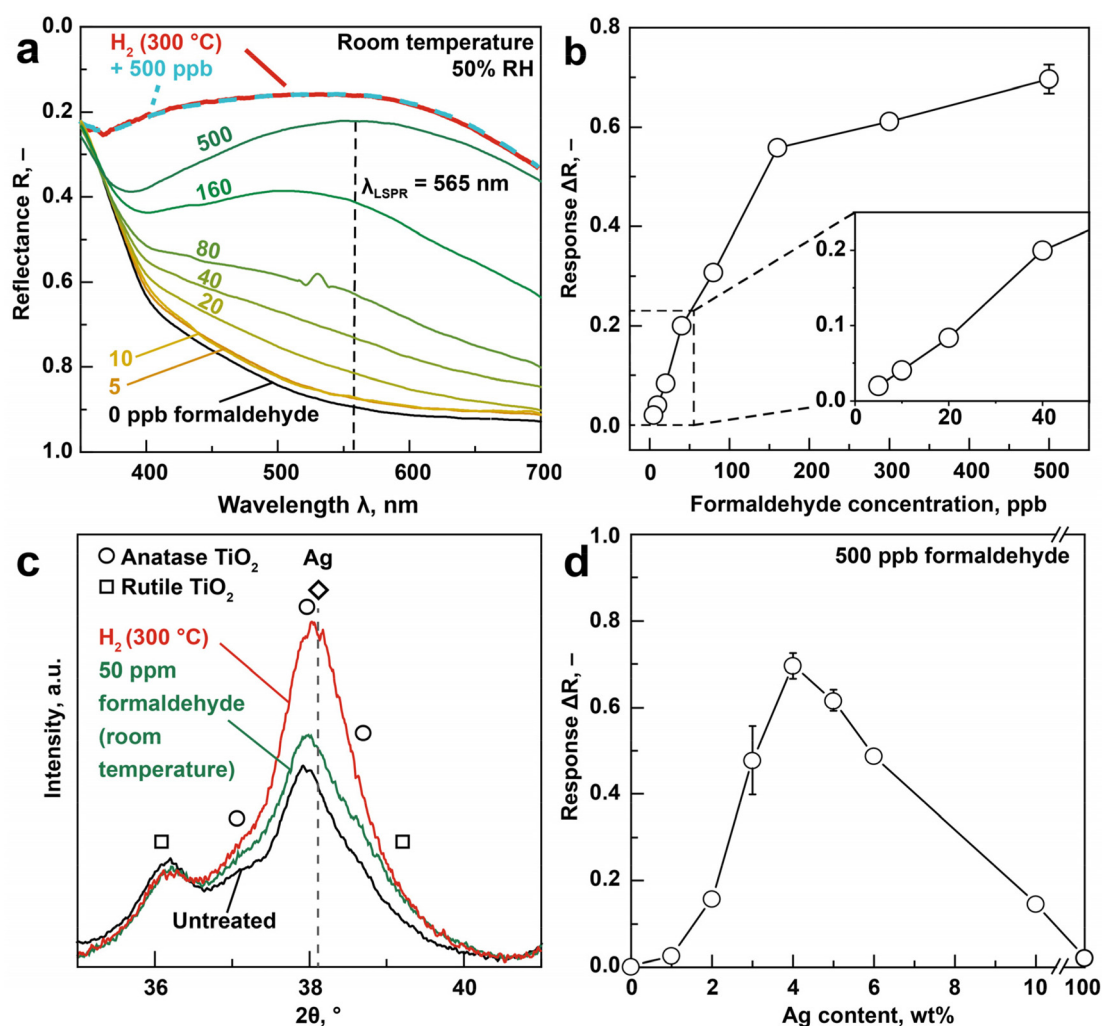

Fig. 2 LSPR formaldehyde sensing and mechanism at room temperature. (a) UV/Vis reflectance spectra (solid lines) of 4 wt% Ag/AgO$_x$–TiO$_2$ nanohybrids when exposed to 0–500 ppb formaldehyde at room temperature and 50% RH in air as well as after reducing the nanohybrids in 5 vol% H$_2$ in Ar at 300 °C for 30 min (red, solid line) and subsequent 500 ppb formaldehyde exposure (turquoise, broken line) that overlap. (b) LSPR response (ΔR at λ_{LSPR} = 565 nm) as a function of formaldehyde concentration (0–500 ppb). (c) Corresponding XRD patterns before (black), after exposure to 50 ppm formaldehyde (green) in air and after reduction with a H$_2$/Ar mixture at 300 °C (red). Reference peaks for metallic Ag (diamond and dashed line), rutile (squares) and anatase (circles) TiO$_2$ are indicated. Extended XRD patterns for 2θ = 22−44° are provided in ESI Fig. 5.† (d) LSPR response (at λ_{LSPR} = 565 nm) of TiO$_2$ with nominal 0−100 wt% Ag to 500 ppb fomaldehyde. Symbols and error bars for 3, 4 and 5 wt% Ag indicate the averages and standard deviations of three identically produced sensors.

relevant range between 0 and 500 ppb (Fig. 2b), covering typical levels in homes (usually <50 ppb),[25] freshly renovated buildings (e.g. 149 ppb for 6000 homes, in China[26]) and even mobile homes, where formaldehyde concentrations can be above 1000 ppb.[27] Such sensors are also quite reproducible (<5% response deviation), as assessed from three identically produced sensors at 500 ppb (error bar in Fig. 2b). Note that these responses are obtained from the UV/Vis spectra after 60 min of formaldehyde exposure. When faster analysis times are required, the time transients for the different concentrations (ESI Fig. 3b†) can be used, as established for chemoresistive sensors.[28] In both cases, however, exposure time needs to be known to determine concentration.

Most remarkably, the plasmonic Ag/AgO_x core–shell on TiO_2 sensor is capable to detect formaldehyde even down to 5 ppb (signal-to-noise ratio >50) with clear discrimination from 0 and 10 ppb. This is sufficiently low to satisfy the WHO guideline (80 ppb (ref. 14)) in residential buildings and meets even strictest limits of 7 and 8 ppb in California[29] and France[30] (beginning in 2023), respectively. This demonstrates the immediate impact of *chemical reaction-mediated* LSPR sensing materials, since several orders of magnitude lower detection limits are achieved than those yielded by conventional LSPR based only on *refractive index sensing*. In fact, similarly prepared flame-made Au-TiO$_2$[11] detected other volatile organic compounds (i.e., ethanol, acetone, toluene) only down to 1 vol% while Au–CuO sensed CO down to 50 ppm.[31] The present detector outperforms even other nanoparticle-based sensor types (e.g. electrochemical, chemoresistive, fluorescence, Table 1) that detected formaldehyde down to 10 ppb, but at unrealistic dry conditions.[32] In fact, comparable formaldehyde concentrations at relevant RH were only detected when *heating* the chemoresistive nanoparticles (e.g. 20 ppb with $In_4Sn_3O_{12}$ at 250 °C with 50% RH,[33] 3 ppb with Si/Pd/Pt or Ti-doped SnO_2 at 400 °C with 90% RH[34]) rendering them less suitable for wearable applications.

This superior LSPR sensitivity of Ag/AgO_x clusters with formaldehyde at room temperature should be attributed to their redox interaction, as shown in Fig. 1a. This is verified by reducing first all surface AgO_x to metallic Ag with 5 vol% H_2 in Ar at 300 °C (ref. 20) (Fig. 2a, red line) yielding a similar plasmonic hump to Ag/AgO_x under formaldehyde exposure (e.g. 500 ppb, dark green line), just more pronounced. Remarkably, this plasmonic hump does not change when exposing it subsequently to 500 ppb formaldehyde (dashed turquoise line that is on top of the red line), due to the already completed reduction to metallic Ag. Therefore, the redox interaction of formaldehyde with Ag/AgO_x is indeed responsible for its highly sensitive LSPR sensing.

We investigated this further by XRD of untreated Ag/AgO_x–TiO_2 (Fig. 2c, black line) and *in situ* upon exposure to 50 ppm formaldehyde at room temperature (green line). Most importantly, the Ag peak (diamond) at $2\theta = 38.1°$ increases upon exposure to 50 ppm formaldehyde, suggesting the growth of Ag crystals from the AgO_x reduction and further verifying our concept (Fig. 1a). Note that this Ag peak overlaps with peaks of anatase TiO_2 (i.e., $2\theta = 37.7°$, circles). However, the TiO_2 is not affected by the formaldehyde exposure, as shown in ESI Fig. 5† where neither the anatase (e.g. at $2\theta = 25.2°$) nor the rutile peaks ($2\theta = 27.4°$) were affected. An even stronger increase in peak intensity at 38.1° (Fig. 2c, red line) was observed after H_2 reduction at 300 °C, in agreement with the UV/Vis spectra in Fig. 2a.

Finally, also the effect of Ag/AgO_x content on the response to 500 ppb of formaldehyde at room temperature and 50% RH is investigated (Fig. 2d). Thereby, flame-made pure TiO_2 features no detectable optical response, as expected. When increasing the Ag/AgO_x content to 4 wt%, a response optimum of 0.69 is observed, as expected from the Beer–Lambert law due to stronger plasmonic light absorption with higher Ag/AgO_x surface loading. Above 4 wt%, however, the response

Table 1 Nanoparticle-based formaldehyde sensors that work at room temperature

Material sensor type	LOQ[e] (RH) [ppb]	RH range	Formaldehyde selectivity									Ref.
			Acetaldehyde	Ethanol	Methanol	Acetone	Benzene	NH$_3$	CO	H$_2$	NO$_2$	
Cr-Pdene/C *electrochemical*	200 (dry)	Dry	—	High	—	—	—	High	—	—	—	57
ZIF-7/TiO$_2$[a] *chemoresistive*	25 (dry)	Dry	—	57	—	>1000	—	>2000	—	>1000		58
MXene/Co$_3$O$_4$ *chemoresistive*	10 (dry)	0–97%	—	11	—	6	13	6	—	—	—	32
Ag—In$_2$O$_3$[b] *chemoresistive*	50 (16%)	16–75%	—	4	6	>100	50	40	—	—	—	63
Ag-FAUY[c] *colorimetric/fluorescence*	80	[d]	—	7	—	—	3.5	—	—	—	—	64
CdSe/ZnS *fluorescence*	500 (dry)	0–85%	—	High	—	High	—	—	—	—	—	65
Ni–In$_2$O$_3$/WS$_2$ *chemoresistive*	50 (dry)	0–97%	—	2	2.5	3	6	2	–	–	3	66
Ag/AgO$_x$–TiO$_2$ *plasmonic*	5 (50%)	0–90%	9.2	600	550	140	>1000	130	950	140	90	This work

[a] Requires UV illumination. [b] Evaluated at nominal 5 wt% Ag. [c] Zeolite faujasite Y-type. [d] Measured at low (but unspecified) RH. Formaldehyde vapor generated through evaporating aqueous solution. [e] Limit of quantification, i.e. lowest quantified concentration.

deteriorates progressively. This can be due to increasing size of Ag/AgO_x clusters at higher Ag contents (as with flame-made $Ag/AgO_x–SiO_2$ [16]) featuring reduced catalytic activity,[35] a trend observed also for other plasmonic noble metal-based gas sensors (e.g. Au for O_2 detection[36]).

Formaldehyde selectivity and robustness to RH

To assess the formaldehyde selectivity of the $Ag/AgO_x–TiO_2$ sensor, it was exposed to acetaldehyde, ethanol, methanol, acetone, benzene, NH_3, CO, H_2 and NO_2 at 500 ppb and 50% RH in air (Fig. 3a), covering a wide range of chemical families relevant for air quality monitoring.[14] Most remarkably, formaldehyde is detected with the highest response (0.69) compared to acetaldehyde (0.075) while all other analytes are hardly detected (≤0.016). This results in outstanding selectivities ranging from over 9 for acetaldehyde to 1300 for benzene.

Noteworthy, this also includes NO_2 and H_2 (140), that are prominent analytes for noble metal LSPR sensors (e.g. Au–CeO_2[3] for NO_2 or $Pd_{70}Au_{30}$[2] for H_2). The sensor's performance is also competitive, if not significantly better, than other nanoparticle-based formaldehyde sensor types that work at room temperature (Table 1). For instance, most of these sensors suffered from rather weak ethanol selectivity (<60), that is particularly problematic given ethanol's omnipresence in cleaning agents or disinfectants,[37] requiring their combination, for example, with filters (e.g. molecular sieves[38] or sorption columns[39]).

This formaldehyde selectivity is related to the selective redox interaction of the formaldehyde with the Ag/AgO_x clusters (Fig. 2a and c), that is supported further by chemical conversion measurements with high resolution proton transfer reaction time-of-flight mass spectrometry (PTR-TOF-MS,
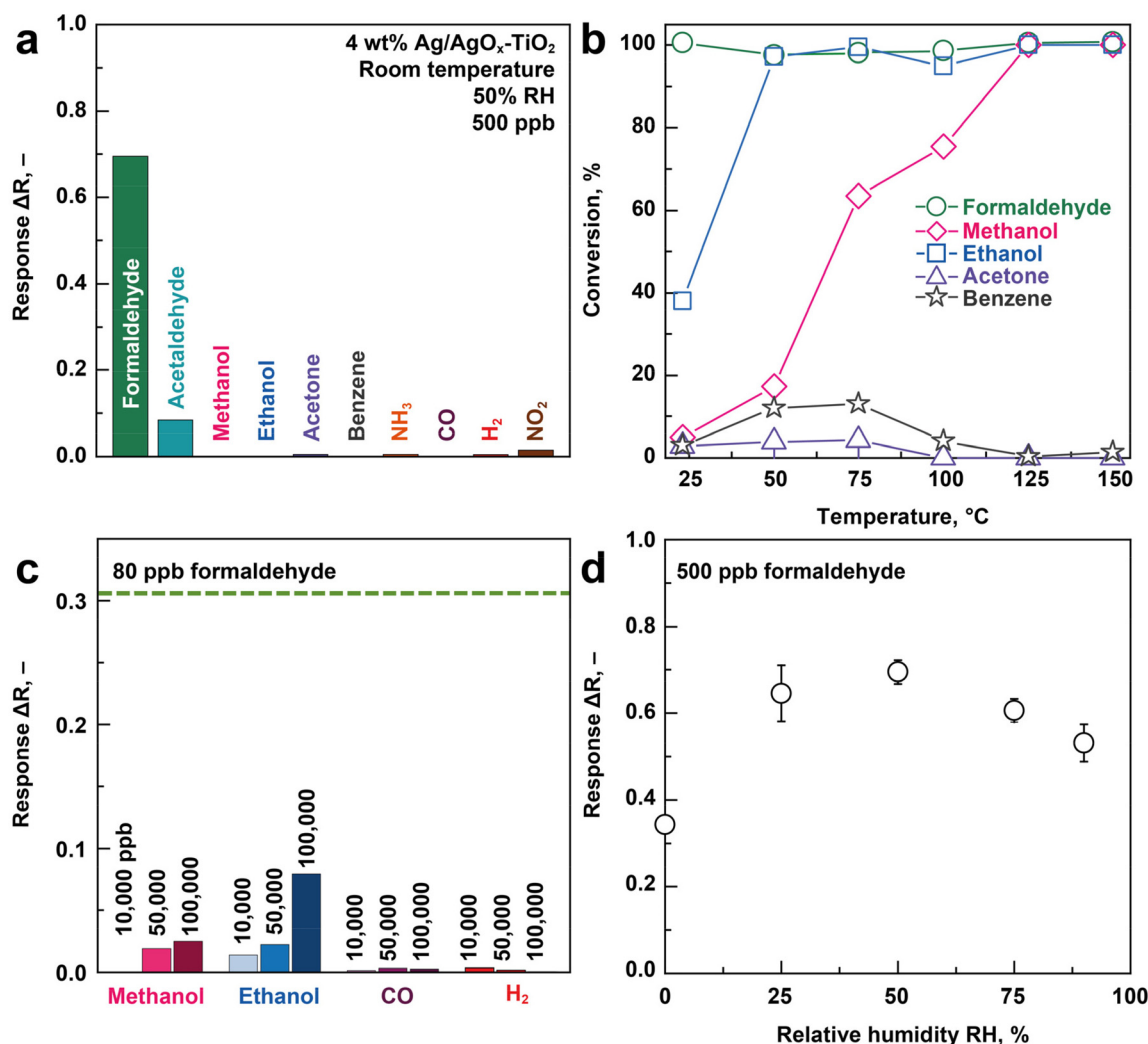

Fig. 3 Selectivity to formaldehyde and humidity robustness at room temperature. (a) LSPR response of 4 wt% Ag/AgO_x on TiO_2 nanohybrids to 500 ppb of various indoor air-relevant gases and vapors at 50% RH in air. (b) Chemical conversion of 1 ppm formaldehyde (circles), methanol (diamonds), ethanol (squares), acetone (triangles) and benzene (stars) at 50% RH over 20 mg of these nanohybrids as a function of temperature. (c) LSPR response to 10 000, 50 000 and 100 000 ppb of methanol, ethanol, CO and H_2. The response to 80 ppb formaldehyde (i.e. current WHO guideline[14]) is shown as dashed line for reference. (d) LSPR response to 500 ppb formaldehyde at various RH.

Fig. 3b). In fact, formaldehyde (circles) is fully converted already at room temperature at 50% RH in air, in agreement with literature.[15] This confirms the chemical reaction for the sensor–analyte interaction. In contrast, ethanol (squares) requires 60 °C for full conversion while acetone and benzene are not even converted completely at 150 °C, in agreement with the sensor results (Fig. 3a). Note that NH_3, CO, H_2 and NO_2 are not analyzed, as these can hardly be detected by PTR-TOF-MS with H_3O^+ primary ions.

To challenge the sensor even further, it is exposed to much higher confounder concentrations (10 000–100 000 ppb) of methanol, ethanol, CO, and H_2 (Fig. 3c), that can be present in indoor air from cleaning agents,[37] combustion sources[40] or emitted from humans.[41] Remarkably, the sensor is hardly affected and features, at least, three times lower response to these confounders compared to more than three orders of magnitude lower formaldehyde concentrations (i.e. 80 ppb, the WHO limit,[14] horizontal dashed line). Thus, the Ag/AgO$_x$–TiO$_2$ sensor is quite robust even to such extreme conditions, where low-cost air quality sensors often fail, as frequently identified as a major challenge by environmental scientists.[42] These results highlight the impact of reaction-mediation to render LSPR sensors highly selective and thereby overcome a long-standing limitation for their application to VOC.

Humidity is another challenge for portable formaldehyde sensors that can vary during air quality monitoring. Most importantly, the formaldehyde redox reaction with Ag/AgO$_x$ is largely humidity-independent (response variation ± 11%) in the relevant[43] range, 25–90% RH, as shown in Fig. 3d. Noteworthy, the Ag/AgO$_x$–TiO$_2$ sensor response nearly doubles

from dry to 25% RH suggesting that water vapor plays a significant role in the redox reaction of formaldehyde with Ag/AgO$_x$. This is in agreement with formaldehyde oxidation catalysts (Ag–TiO$_2$[15] and Pt–TiO$_2$[44]) at room temperature that increased conversion efficiencies at elevated RH. This was attributed there to increased density of hydroxyl reaction sites.

Wearable device

To demonstrate the immediate practical impact of the formaldehyde sensor, a white fabric (diameter 15 mm, serving also as white balance reference) is coated with these LSPR nanoparticles and mounted onto a wearable wristband (Fig. 4a). The film morphology evaluated by scanning electron microscopy is shown in ESI Fig. 6.† Such films are highly accessible to analytes due to their high porosity, a distinct advantage of flame aerosol deposited sensing films.[45] A smartphone camera is applied for formaldehyde quantification by evaluating the color change upon formaldehyde exposure. Thereby, the color difference (ΔE) is indicated in the $L^*a^*b^*$ color space,[46] according to ISO 11664-4. This method is more objective than an assessment by human eye and user-friendly, given the large availability of smartphones (global penetration rate: 67% in 2020).[47] Most importantly, neither bulky UV/vis spectrometers nor other auxiliary systems are required, such as batteries[8] or pumps[48] that are quite standard in handheld devices with other sensor types (e.g. heated chemoresistors).

Fig. 4b shows images of the sensor after exposure to 0, 80 and 500 ppb formaldehyde at 50% RH and room temperature. Remarkably, a color change from beige to brownish is visible even by naked eye already at the WHO limit of 80 ppb that
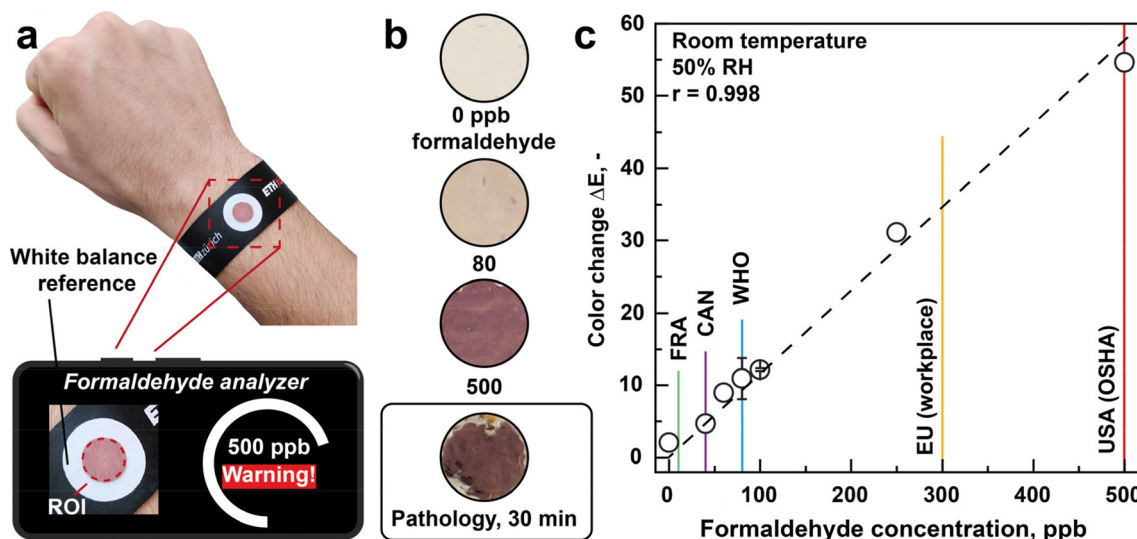

Fig. 4 Sensor integration into wearable device and smartphone read-out. (a) Image of the plasmonic sensing film coated onto a white glass fiber substrate and mounted onto a flexible wristband. The ambient formaldehyde concentration is quantified by a smartphone camera and visualized on a smartphone. (b) Images of these films when exposed to 0, 80 and 500 ppb of formaldehyde at room temperature and 50% RH in air, as well as to the emissions of a dilute formalin solution bath for tissue fixation in the pathology of a local hospital. (c) Color change as quantified by the image processing algorithm in response to 0–500 ppb formaldehyde. The corresponding ideal line (dashed black) and the Pearson correlation coefficient (r) are indicated. The formaldehyde guidelines set by France (8 ppb),[30] Canada (40 ppb),[67] the WHO (80 ppb),[14] the EU workplace limit (300 ppb)[68] and the OSHA action level (500 ppb)[69] are shown as well.

turns to brownish/purple at 500 ppb. This is in agreement with the increasing plasmonic peak between 400 and 700 nm, as observed by UV/Vis reflectance in Fig. 2a. With a smartphone camera, the entire range of relevant formaldehyde concentrations between 40 to 500 ppb is recognized accurately (Fig. 4c). Thereby, the color change ΔE correlates rather linearly (Pearson correlation coefficient r = 0.998) with the formaldehyde concentration. Also, this method is quite reproducible (*i.e.* ±25% at 80 ppb), that is remarkable considering the application of an ordinary smartphone here.

This sensor can be worn as patch to indicate formaldehyde concentration (and possibly also exposure, if applied as dosimeter) in critical workplaces (*e.g.* textile and furniture industry, mortuaries, pathology rooms[25]) to mitigate health risks and improve occupational safety. In fact, an early field test in the pathology of a local hospital demonstrates the recognition of a harmful event under real condition. After 30 min of exposure to the emissions of a diluted formalin solution bath (as typical for tissue fixation), the sensor turned brownish/purple (Fig. 4b). The color change is quite identical to that of 500 ppb of formaldehyde from laboratory standards, that corresponds to the maximum detectable concentration (ESI Fig. 3b†) of this sensor. Simultaneous sampling and off-site analysis measurements by high-resolution proton transfer time-of-flight mass spectrometry quantified the formaldehyde concentration as 10.3 ppm. Note, however, that more validation will be required and we observed some loss of sensing film close to the rim of the glass fiber substrate when the tester moved it to the pathology. While this did not compromise sensor performance, it indicates poor coating stability that needs to be improved.

We envision the use of these Ag/AgO$_x$–TiO$_2$ nanoparticle films also as inexpensive, chemoresponsive paints or coatings, for instance, in "smart" buildings where they can serve as indicators when threshold limits are exceeded (Fig. 4c). Finally, such LPSR sensors are promising also for outdoor applications, where formaldehyde is an increasing concern when emitted at elevated concentrations from "green" fuels[49] or wildfires.

Conclusions

A wearable plasmonic gas sensor for formaldehyde detection was presented that challenges existing sensing technologies for this important air pollutant (Table 1). Most attractive are the detector's room temperature operation, low cost and simple application by smartphone read-out. This was achieved by tailoring Ag/AgO$_x$ core–shell clusters on TiO$_2$ nanoparticles that interact selectively with formaldehyde through a redox reaction. That way, even the lowest formaldehyde concentrations were detected, covering a wide range of current and upcoming national exposure thresholds. This sensor was also highly selective, as demonstrated on various classes of air quality-relevant chemicals including other aldehydes, alcohols, ketones, aromatics, inorganics, and quite robust to RH changes.

In a wider perspective, this work described the next generation of high-performance LSPR sensors that utilize chemical reaction mediation. To date, this concept has been applied only for few inorganic analytes (*e.g.* H$_2$ with Pd, NO$_2$ with Au). Here, it was shown for a highly relevant VOC that opens new avenues for highly selective and sensitive LSPR sensing in emerging applications like air quality control, health monitoring[7] and food safety.[6]

Methods

Sensing nanoparticle preparation

Ag/AgO$_x$–TiO$_2$ nanohybrids with nominal 0–100 wt% Ag were made with a flame spray pyrolysis reactor, described in detail elsewhere.[50] The precursor consisted[19] of titanium(IV) isopropoxide (Sigma Aldrich, 97%) and silver acetate (Sigma Aldrich, >99%), that were diluted in a 1 : 1 (v/v) mixture of acetonitrile (Sigma Aldrich, 99.8%) and 2-ethylhexanoic acid (Sigma Aldrich, 99%) to a total metal content (Ag + Ti) of 0.2 M. For comparison, also Ag/AgO$_x$–SiO$_2$ nanohybrids were made with nominal 4 wt% Ag following the same method. This precursor contained hexamethyldisiloxane (Sigma Aldrich, ≥98%) instead of titanium(IV) isopropoxide, while the rest remained the same.[20] These precursor solutions were fed through a capillary at 5 mL min^{-1} and dispersed with 5 L min^{-1} oxygen (pressure drop across the nozzle: 1.6 bar). A ring-shaped[51] premixed flame of CH$_4$ (1.25 L min^{-1}) and O$_2$ (3.25 L min^{-1}) surrounding the nozzle ignited and sustained the spray flame. Additional 5 L min^{-1} of sheath O$_2$ supplied through an annulus surrounding the flame ensured excess oxidant.

The particles were deposited for 16 min onto a water-cooled glass fiber filter[50] (GF6, Hahnemühle Fineart, 257 mm diameter) at a height of 57 cm above the nozzle aided by a vacuum pump (Seco SV 1025 C, Busch). Sensors were obtained by cutting out 6 mm (diameter) circles of that particle-laden filter with a punching iron (Brütsch, Rüegger & Co.). For some analyses, as specified in the text, powders were obtained by scraping off particles from the filter with a spatula and subsequent sieving (mesh 300 μm, stainless steel) to remove filter fibers. For thermal stabilization and removal of uncombusted precursor, both sensors and powders were annealed at 500 °C for 5 h in an oven (CWF 1300, Carbolite Gero).

Powder and film characterization

STEM of powders was performed on an aberration-corrected HD-2700CS (Hitachi) operated at 200 kV. STEM images were obtained with a HAADF detector with bright Z contrast. EDX-STEM was performed on a Talos F200X (Super-X EDX, 4 detector configuration, FEI) operated at 200 kV. The data were processed using the software Velox 3.0.0.815 (ThermoFisher/FEI).

The XRD patterns of powders were acquired with a Bruker AXS D8 Advance diffractometer operated at 40 kV and 30 mA (Fig. 1c) or a Bruker D2 Phaser operated at 30 kV and 10 mA (Fig. 2c and ESI Fig. 5†) at 2Θ (Cu K$_\alpha$) between 20 to 70°. The

scanning step size and time were 0.012° and 2.25 s, respectively. Crystal phases were identified by comparison to structural parameters of cubic Ag (PDF 4-784), cubic Ag_2O (PDF 75-1532), anatase TiO_2 (PDF 21-1272), rutile TiO_2 (PDF 21-1276), monoclinic Ti_3O_5 (PDF 82-1138) and triclinic Ti_4O_7 (PDF 77-1391). Crystal sizes and weight fractions were approximated by Rietveld refinement with the software Topas 4.2 (Bruker).

The XRD analyses were carried out also immediately after reduction in formaldehyde or H_2. Therefore, 20 mg of 4 wt% Ag/AgO_x–TiO_2 powder was placed in a quartz glass tube and fixed as a packed bed with quartz wool plugs. The formaldehyde reduction was achieved by bubbling 100 ml min^{-1} dry synthetic air (PanGas 99.999%, $C_nH_m \leq 0.1$ ppm, $NO_x \leq 0.1$ ppm) through an aqueous formaldehyde solution (0.265 M, yielding a formaldehyde concentration of 50 ppm in its headspace[52]) and guiding the off-gas through the packed bed for 2 h at room temperature (i.e. 23 °C). The solution was prepared by depolymerizing 0.596 g paraformaldehyde (97%, Sigma Aldrich) in 75 ml H_2O, aided by addition of 250 µl KOH (0.1 M, Sigma Aldrich) at 50 °C for 15 min. Reduction by H_2[20] was carried out by heating the powder in the quartz glass tube to 300 °C under N_2 at 100 ml min^{-1} and exposing it subsequently to 5 vol% H_2 in Ar for 30 min.

The specific surface area (SSA) of powders was determined by nitrogen absorption (Tristar II Plus, Micromeritics) with a Brunauer–Emmett–Teller (BET) five-point method. Prior to measurement, samples were degassed under vacuum for 1 h to remove surface-adsorbed species. Sphere-equivalent diameters were determined from the XRD-derived phase composition using the densities of anatase (3.8 g cm^{-3}), rutile (4.2 g cm^{-3}) and with its nominal content of silver (10.49 g cm^{-3}).

Microscopy was carried out with a FE-SEM 4000 (Hitachi) operated at 12 kV to determine the film morphology and thickness. The film thickness was measured at 16 points around the cut out sensor using the software ImageJ.

LSPR characterization

Gas mixtures were prepared with a mixing set-up described in detail elsewhere.[53] Briefly, analyte gases were supplied from calibrated standards (all PanGas): acetone (15 ppm), benzene (15 ppm), CO (500 ppm), ethanol (15 and 500 ppm), formaldehyde (15 ppm), H_2 (50 and 1000 ppm) and NO_2 (10 ppm), all in synthetic air except for the formaldehyde that was in N_2 (due to its limited stability in air). These were diluted with hydrocarbon-free synthetic air (PanGas 99.999%, $C_nH_m \leq 0.1$ ppm, $NO_x \leq 0.1$ ppm) with high-resolution and calibrated mass flow controllers (EL-FLOW Select, Bronkhorst). Humidity was added by bubbling synthetic air through distilled water and admixed to the analyte stream to achieve the desired RH. Thereby, the RH (e.g. 50.5 ± 0.3% during 48 h, ESI Fig. 7†) and temperature (22 ± 0.2 °C) of the resulting gas stream were closely maintained at set values, as continuously checked with a SHT2x sensor (Sensirion AG) and in good agreement to literature.[54] The total flow rate was 300 mL min^{-1}.

For UV/vis experiments, a diffuse reflectance set-up was used, as standard[55] for the measurement of such optical pro-

perties. Therefore, the sensors were placed inside a Praying Mantis diffuse reflection accessory equipped with a reaction chamber (both Harrick Sci.) and connected to the above gas mixing set-up. The sensors were operated at 31 °C, as measured by a K-type thermocouple. Diffuse reflectance spectra were obtained with a Varian Cary 500 UV/Vis-NIR spectrophotometer (Bruker) between 350 to 700 nm using an averaging time of 2 s and step size of 1 nm. A particle-free glass fibre substrate served as the background. The reflectance difference (ΔR) served as sensor response:[56]

$$\Delta R = R_{analyte} - R_{air}$$

with R_{air} and $R_{analyte}$ being the reflectances in air and with analyte exposure, respectively. The formaldehyde selectivity was defined as the ratio of the formaldehyde response $R_{formaldehyde}$ to the response of another analyte $R_{analyte}$, in agreement with literature.[57,58]

Catalytic conversion

The catalytic conversion was assessed with a custom-built[59] set-up. In brief, 20 mg of 4 wt% Ag/AgO_x–TiO_2 powder was filled into a glass tube and fixed as a packed bed with quartz wool. The glass tube was placed inside a horizontal oven (Carbolite EZS 12/450) and connected to the aforementioned gas mixing set-up at a total flow rate of 150 mL min^{-1} and 50% RH. The off-gas was monitored in real-time using a PTR-ToF-MS (Ionicon PTR-ToF-MS 1000) operated with a drift voltage, temperature, and pressure of 600 V, 60 °C and 2.3 mbar, respectively. In the drift tube, the reduced electric field (E/N) was 130 Td. H_3O^+ was used as primary ion. The respective analyte concentrations were observed at a mass-to-charge (m/z) ratio of 31.018 (ref. 60) (formaldehyde), 47.049 (ref. 60) (ethanol), 59.045 (ref. 61) (acetone) and 79.051 (ref. 61) (benzene). Before every measurement, the PTR-ToF-MS was five-point calibrated over the range of 0 and 1000 ppb using the aforementioned gas standards. The gas conversion was calculated using

$$C = 1 - \frac{outlet\ conc.}{inlet\ conc.}.$$

Wearable integration and smartphone read-out

The wearable wristband was fabricated by attaching the sensing film with double-sided Kapton tape onto white paper (15 mm diameter) that served as white balance. This was then mounted on a paper wristband. Images of the sensor films were taken with flashlight in the beginning and after 60 min of formaldehyde exposure with a smartphone camera (OnePlus 7T). The images were evaluated using a tailor-made MatLab code. Essentially, the algorithm applies a white balance for each image with respect to the white paper background to mitigate effects of varying lighting conditions. The image is converted into the $L^*a^*b^*$ color space, as defined by the International Commission on Illumination. A region of interest is chosen on the sensing film where the mean values of L^*, a^*, and b^* are calculated. Following the norm EN ISO 11664-4,

the color difference (ΔE, *i.e.* sensor response) is calculated as the Euclidean distance between the image before and with analyte exposure:

$$\Delta E = \sqrt{\left(L_{air} - L_{analyte}\right)^2 + \left(a_{air} - a_{analyte}\right)^2 + \left(b_{air} - b_{analyte}\right)^2}.$$

Early field tests were carried out in the pathology of a local hospital. Before the test, a sensor was stored in synthetic air and at 50% RH. In the pathology, the sensor was placed on a workbench at 20 cm distance from a 4 vol% formalin solution bath for tissue fixation and exposed for 30 min to the surrounding air. For benchmarking, air was sampled simultaneously into Tedlar bags (3 L, SKC Inc.) co-located to the sensor using a pump and analyzed within 2 h by PTR-ToF-MS to prevent analyte loss through the bag wall. Gas samples were diluted with synthetic air at 50% RH to avoid instrument saturation. Note that the Tedlar bags had been cleaned before use by pulling vacuum and filling them with nitrogen (PanGas 99.999%) for three times.[62]

Data availability

The data that support the findings of this study can be requested from the corresponding author.

Author contributions

Conflicts of interest

The authors declare no conflict of interest.

Acknowledgements

References

1 A. Tittl, H. Giessen and N. Liu, Plasmonic gas and chemical sensing, *Nanophotonics*, 2014, **3**(3), 157–180.

2 F. A. A. Nugroho, I. Darmadi, L. Cusinato, A. Susarrey-Arce, H. Schreuders, L. J. Bannenberg, A. B. da Silva Fanta, S. Kadkhodazadeh, J. B. Wagner, T. J. Antosiewicz, A. Hellman, V. P. Zhdanov, B. Dam and C. Langhammer, Metal-polymer hybrid nanomaterials for plasmonic ultrafast hydrogen detection, *Nat. Mater.*, 2019, **18**(5), 489–495.

3 N. A. Joy, M. I. Nandasiri, P. H. Rogers, W. Jiang, T. Varga, S. V. N. T. Kuchibhatla, S. Thevuthasan and M. A. Carpenter, Selective Plasmonic Gas Sensing: H$_2$, NO$_2$, and CO Spectral Discrimination by a Single Au-CeO$_2$ Nanocomposite Film, *Anal. Chem.*, 2012, **84**(11), 5025–5034.

4 I. Darmadi, F. A. A. Nugroho and C. Langhammer, High-Performance Nanostructured Palladium-Based Hydrogen Sensors—Current Limitations and Strategies for Their Mitigation, *ACS Sens.*, 2020, **5**(11), 3306–3327.

5 I. Tanyeli, I. Darmadi, M. Sech, C. Tiburski, J. Fritzsche, O. Andersson and C. Langhammer, Nanoplasmonic NO2 Sensor with a Sub-10 Parts per Billion Limit of Detection in Urban Air, *ACS Sens.*, 2022, **7**(4), 1008–1018.

6 M. Mayer and A. J. Baeumner, A Megatrend Challenging Analytical Chemistry: Biosensor and Chemosensor Concepts Ready for the Internet of Things, *Chem. Rev.*, 2019, **119**(13), 7996–8027.

7 A. T. Güntner, S. Abegg, K. Konigstein, P. A. Gerber, A. Schmidt-Trucksass and S. E. Pratsinis, Breath Sensors for Health Monitoring, *ACS Sens.*, 2019, **4**(2), 268–280.

8 S. Abegg, L. Magro, J. van den Broek, S. E. Pratsinis and A. T. Güntner, A pocket-sized device enables detection of methanol adulteration in alcoholic beverages, *Nat. Food*, 2020, **1**(6), 351–354.

9 K. A. Willets and R. P. V. Duyne, Localized Surface Plasmon Resonance Spectroscopy and Sensing, *Annu. Rev. Phys. Chem.*, 2007, **58**(1), 267–297.

10 W. M. Haynes, *CRC handbook of chemistry and physics*, CRC press, Boca Raton, U.S.A., 2014.

11 Z. Fusco, M. Rahmani, R. Bo, R. Verre, N. Motta, M. Kall, D. Neshev and A. Tricoli, Nanostructured Dielectric Fractals on Resonant Plasmonic Metasurfaces for Selective and Sensitive Optical Sensing of Volatile Compounds, *Adv. Mater.*, 2018, **30**(30), e1800931.

12 International Agency for Research on Cancer, *IARC classifies formaldehyde as carcinogenic to humans*. IARC, Lyon, 2004.

13 M. Böhm, M. Z. M. Salem and J. Srba, Formaldehyde emission monitoring from a variety of solid wood, plywood, blockboard and flooring products manufactured for building and furnishing materials, *J. Hazard. Mater.*, 2012, **221–222**, 68–79.

14 World Health Organization, *WHO guidelines for indoor air quality: selected pollutants*. WHO, Bonn, 2010.

15 R. Fang, M. He, H. Huang, Q. Feng, J. Ji, Y. Zhan, D. Y. C. Leung and W. Zhao, Effect of redox state of Ag on indoor formaldehyde degradation over Ag/TiO$_2$ catalyst at room temperature, *Chemosphere*, 2018, **213**, 235–243.

16 C. Gunawan, W. Y. Teoh, C. P. Marquis, J. Lifia and R. Amal, Reversible Antimicrobial Photoswitching in Nanosilver, *Small*, 2009, **5**(3), 341–344.

17 B. Tollens, Ueber ammon–alkalische Silberlösung als Reagens auf Aldehyd, *Ber. Dtsch. Chem. Ges.*, 1882, **15**(2), 1635–1639.

18 L. Guo, H. Yin, M. Xu, Z. Zheng, X. Fang, R. Chong, Y. Zhou, L. Xu, Q. Xu, J. Li and H. Li, In Situ Generated Plasmonic Silver Nanoparticle-Sensitized Amorphous Titanium Dioxide for Ultrasensitive Photoelectrochemical Sensing of Formaldehyde, *ACS Sens.*, 2019, **4**(10), 2724–2729.

19 K. Fujiwara, Y. Deligiannakis, C. G. Skoutelis and S. E. Pratsinis, Visible-light active black TiO$_2$-Ag/TiOx particles, *Appl. Catal., B*, 2014, **154–155**(0), 9–15.

20 G. A. Sotiriou, A. Meyer, J. T. Knijnenburg, S. Panke and S. E. Pratsinis, Quantifying the origin of released Ag + ions from nanosilver, *Langmuir*, 2012, **28**(45), 15929–15936.

21 P. Kubelka and F. Munk, Ein Beitrag zur Optik der Farbanstriche, *Z. Tech. Phys.*, 1931, **12**, 593–601.

22 S. Peng, J. M. McMahon, G. C. Schatz, S. K. Gray and Y. Sun, Reversing the size-dependence of surface plasmon resonances, *Proc. Natl. Acad. Sci. U. S. A.*, 2010, **107**(33), 14530–14534.

23 R. C. Shannon, B. Lafuente, R. D. Shannon, R. T. Downs and R. X. Fischer, Refractive indices of minerals and synthetic compounds, *Am. Mineral.*, 2017, **102**(9), 1906–1914.

24 Y. Ohko, T. Tatsuma, T. Fujii, K. Naoi, C. Niwa, Y. Kubota and A. Fujishima, Multicolour photochromism of TiO$_2$ films loaded with silver nanoparticles, *Nat. Mater.*, 2003, **2**(1), 29–31.

25 T. Salthammer, S. Mentese and R. Marutzky, Formaldehyde in the indoor environment, *Chem. Rev.*, 2010, **110**(4), 2536–2572.

26 X. Tang, Y. Bai, A. Duong, M. T. Smith, L. Li and L. Zhang, Formaldehyde in China: Production, consumption, exposure levels, and health effects, *Environ. Int.*, 2009, **35**(8), 1210–1224.

27 K. Sexton, M. X. Petreas and K. S. Liu, Formaldehyde exposures inside mobile homes, *Environ. Sci. Technol.*, 1989, **23**(8), 985–988.

28 T. Hibbard, K. Crowley, F. Kelly, F. Ward, J. Holian, A. Watson and A. J. Killard, Point of care monitoring of hemodialysis patients with a breath ammonia measurement device based on printed polyaniline nanoparticle sensors, *Anal. Chem.*, 2013, **85**(24), 12158–12165.

29 California Office of environmental health hazard assessment, *Air Toxics Hot Spots Risk Assessment Guidelines: Appendix D. Individual acute, 8-hour, and chronic reference exposure level summaries*, Sacramento, 2008.

30 Ministère de L'Écoologie, du Développement Durable, des Transports et du Logement, *Décret n° 2011-1727 du 2 Décembre 2011 Relatif aux Valeurs-Guides Pour L'air Intérieur pour le Formaldéhyde et le Benzène*. Paris, 2011.

31 M. Ando, T. Kobayashi, S. Iijima and M. Haruta, Optical CO sensitivity of Au–CuO composite film by use of the plasmon absorption change, *Sens. Actuators B*, 2003, **96**(3), 589–595.

32 D. Zhang, Q. Mi, D. Wang and T. Li, MXene/Co$_3$O$_4$ composite based formaldehyde sensor driven by ZnO/MXene nanowire arrays piezoelectric nanogenerator, *Sens. Actuators B*, 2021, **339**, 129923.

33 J. A. Kemmler, S. Pokhrel, J. Birkenstock, M. Schowalter, A. Rosenauer, N. Bârsan, U. Weimar and L. Mädler, Quenched, nanocrystalline In$_4$Sn$_3$O$_{12}$ high temperature phase for gas sensing applications, *Sens. Actuators B*, 2012, **161**(1), 740–747.

34 A. T. Güntner, V. Koren, K. Chikkadi, M. Righettoni and S. E. Pratsinis, E-Nose, Sensing of Low-ppb Formaldehyde in Gas Mixtures at High Relative Humidity for Breath Screening of Lung Cancer?, *ACS Sens.*, 2016, **1**(5), 528–535.

35 C.-F. Mao and M. A. Vannice, Formaldehyde oxidation over Ag catalysts, *J. Catal.*, 1995, **154**(2), 230–244.

36 P. H. Rogers and M. A. Carpenter, Particle size sensitivity dependence of nanocomposites for plasmonic-based all-optical sensing applications, *J. Phys. Chem. C*, 2010, **114**(25), 11033–11039.

37 V. Bessonneau and O. Thomas, Assessment of exposure to alcohol vapor from alcohol-based hand rubs, *Int. J. Environ. Res. Public Health*, 2012, **9**(3), 868–879.

38 A. T. Güntner, S. Abegg, K. Wegner and S. E. Pratsinis, Zeolite membranes for highly selective formaldehyde sensors, *Sens. Actuators B*, 2018, **257**, 916–923.

39 J. van den Broek, D. K. Cerrejon, S. E. Pratsinis and A. T. Güntner, Selective formaldehyde detection at ppb in indoor air with a portable sensor, *J. Hazard. Mater.*, 2020, 123052.

40 Y. B. De Bruin, P. Carrer, M. Jantunen, O. Hänninen, G. S. Di Marco, S. Kephalopoulos, D. Cavallo and M. Maroni, Personal carbon monoxide exposure levels: contribution of local sources to exposures and microenvironment concentrations in Milan, *J. Exposure Sci. Environ. Epidemiol.*, 2004, **14**(4), 312–322.

41 J. A. Perman, S. Modler, R. G. Barr and P. Rosenthal, Fasting breath hydrogen concentration: normal values and clinical application, *Gastroenterology*, 1984, **87**(6), 1358–1363.

42 A. Lewis and P. Edwards, Validate personal air-pollution sensors, *Nature*, 2016, **535**(7610), 29–31.

43 J. L. Nguyen and D. W. Dockery, Daily indoor-to-outdoor temperature and humidity relationships: a sample across seasons and diverse climatic regions, *Int. J. Biometeorol.*, 2016, **60**(2), 221–229.

44 D. W. Kwon, P. W. Seo, G. J. Kim and S. C. Hong, Characteristics of the HCHO oxidation reaction over Pt/TiO$_2$ catalysts at room temperature: The effect of relative humidity on catalytic activity, *Appl. Catal., B*, 2015, **163**, 436–443.

45 A. T. Güntner, N. J. Pineau and S. E. Pratsinis, Flame-made chemoresistive gas sensors and devices, *Prog. Energy Combust. Sci.*, 2022, **90**, 100992.

46 J. Schanda, *Colorimetry: understanding the CIE system*, John Wiley & Sons, 2007.

47 United Nations; Statista; Ericsson, Global smartphone penetration rate as share of population from 2016 to 2020. 2021, https://www.statista.com/statistics/203734/global-smartphone-penetration-per-capita-since-2005/.

48 I. C. Weber, P. Rüedi, P. Šot, A. T. Güntner and S. E. Pratsinis, Handheld Device for Selective Benzene Sensing over Toluene and Xylene, *Adv. Sci.*, 2022, **9**(4), 2103853.

49 J. C. Liao, L. Mi, S. Pontrelli and S. Luo, Fuelling the future: microbial engineering for the production of sustainable biofuels, *Nat. Rev. Microbiol.*, 2016, **14**(5), 288–304.

50 L. Mädler, H. K. Kammler, R. Mueller and S. E. Pratsinis, Controlled synthesis of nanostructured particles by flame spray pyrolysis, *J. Aerosol Sci.*, 2002, **33**(2), 369–389.

51 L. Mädler, W. J. Stark and S. E. Pratsinis, Flame-made Ceria Nanoparticles, *J. Mater. Res.*, 2002, **17**(6), 1356–1362.

52 S. Dong and P. K. Dasgupta, Solubility of gaseous formaldehyde in liquid water and generation of trace standard gaseous formaldehyde, *Environ. Sci. Technol.*, 1986, **20**(6), 637–640.

53 A. T. Güntner, M. Righettoni and S. E. Pratsinis, Selective sensing of NH_3 by Si-doped α-MoO_3 for breath analysis, *Sens. Actuators B*, 2016, **223**, 266–273.

54 A. T. Güntner, M. Wied, N. J. Pineau and S. E. Pratsinis, Rapid and Selective NH_3 Sensing by Porous CuBr, *Adv. Sci.*, 2020, **7**(7), 1903390.

55 P. Makuła, M. Pacia and W. Macyk, How To Correctly Determine the Band Gap Energy of Modified Semiconductor Photocatalysts Based on UV–Vis Spectra, *J. Phys. Chem. Lett.*, 2018, **9**(23), 6814–6817.

56 E. Herkert, F. Sterl, N. Strohfeldt, R. Walter and H. Giessen, Low-Cost Hydrogen Sensor in the ppm Range with Purely Optical Readout, *ACS Sens.*, 2020, **5**(4), 978–983.

57 J. Zhang, F. Lv, Z. Li, G. Jiang, M. Tan, M. Yuan, Q. Zhang, Y. Cao, H. Zheng, L. Zhang, C. Tang, W. Fu, C. Liu, K. Liu, L. Gu, J. Jiang, G. Zhang and S. Guo, Cr-Doped Pd Metallene Endows a Practical Formaldehyde Sensor New Limit and High Selectivity, *Adv. Mater.*, 2022, **34**(2), 2105276.

58 Y. K. Jo, S.-Y. Jeong, Y. K. Moon, Y.-M. Jo, J.-W. Yoon and J.-H. Lee, Exclusive and ultrasensitive detection of formaldehyde at room temperature using a flexible and monolithic chemiresistive sensor, *Nat. Commun.*, 2021, **12**(1), 4955.

59 A. T. Güntner, I. C. Weber and S. E. Pratsinis, Catalytic Filter for Continuous and Selective Ethanol Removal Prior to Gas Sensing, *ACS Sens.*, 2020, **5**(4), 1058–1067.

60 K. Schwarz, A. Pizzini, B. Arendacka, K. Zerlauth, W. Filipiak, A. Schmid, A. Dzien, S. Neuner, M. Lechleitner, S. Scholl-Burgi, W. Miekisch, J. Schubert, K. Unterkofler, V. Witkovsky, G. Gastl and A. Amann, Breath acetone-aspects of normal physiology related to age and gender as determined in a PTR-MS study, *J. Breath Res.*, 2009, **3**(2), 027003.

61 M. Müller, T. Mikoviny, S. Feil, S. Haidacher, G. Hanel, E. Hartungen, A. Jordan, L. Märk, P. Mutschlechner, R. Schottkowsky, P. Sulzer, J. H. Crawford and A. Wisthaler, A compact PTR-ToF-MS instrument for airborne measurements of volatile organic compounds at high spatiotemporal resolution, *Atmos. Meas. Tech.*, 2014, **7**(11), 3763–3772.

62 J. van den Broek, D. Bischof, N. Derron, S. Abegg, P. A. Gerber, A. T. Güntner and S. E. Pratsinis, Screening Methanol Poisoning with a Portable Breath Detector, *Anal. Chem.*, 2021, **93**(2), 1170–1178.

63 S. Zhou, M. Chen, Q. Lu, Y. Zhang, J. Zhang, B. Li, H. Wei, J. Hu, H. Wang and Q. Liu, Ag Nanoparticles Sensitized In_2O_3 Nanograin for the Ultrasensitive HCHO Detection at Room Temperature, *Nanoscale Res. Lett.*, 2019, **14**(1), 365.

64 D. Yao, Y. Wang and H. Li, Silver clusters based sensor for Low content formaldehyde detection in colorimetric and fluorometric dual Mode, *Sens. Actuators B*, 2020, **305**, 127451.

65 S. Xue, X.-F. Jiang, G. Zhang, H. Wang, Z. Li, X. Hu, M. Chen, T. Wang, A. Luo, H.-p. Ho, S. He and X. Xing, Surface Plasmon-Enhanced Optical Formaldehyde Sensor Based on CdSe@ZnS Quantum Dots, *ACS Sens.*, 2020, **5**(4), 1002–1009.

66 D. Zhang, Y. Cao, Z. Yang and J. Wu, Nanoheterostructure Construction and DFT Study of Ni-Doped In2O3 Nanocubes/WS2 Hexagon Nanosheets for Formaldehyde Sensing at Room Temperature, *ACS Appl. Mater. Interfaces*, 2020, **12**(10), 11979–11989.

67 Government of Canada, *Residential Indoor Air Quality Guideline: Formaldehyde*, Ottawa, 2006.

68 European Parliament and Council, DIRECTIVE 2004/37/EC. *Official Journal of the European Unio*n, 2004.

69 Occupational Safety and Health Administration, Standard Number: 1910.1048 - Formaldehyde. *Occupational Safety and Health Standards* 2013.